Effect of Synthesis Conditions on the Composition, Local Structure and Electrochemical Behavior of (Cr,Fe,Mn,Co,Ni)$_3$O$_4$ Anode Material

Kseniya V. Mishchenko,[a] Pavel Yu. Tyapkin,[a] Arseny B. Slobodyuk,[a, b] Maria A. Kirsanova,[c] and Nina V. Kosova*[a]

Disordered high entropy spinels (HES) (Cr,Fe,Mn,Co,Ni)$_3$O$_4$ were obtained by solid-state synthesis and co-precipitation using various powder precursors. They were characterized by a complex of physico-chemical methods and investigated as anode materials for lithium-ion batteries (LIBs). According to XRD and TEM data, the materials are single-phase. The structural characterization of the samples obtained at 773, 973, and 1273 K was determined using Raman and Mössbauer spectroscopy, and magnetic measurements. The degree of spinel inversion and lattice distortion (microstrains) decrease with increasing synthesis temperature, while the crystallite size increases. The insufficient nickel content in the samples ensures a more uniform distribution of iron cations in both sublattices, which leads to an increase in the lattice parameters and has a positive effect on the de-/lithiation. Repeated ball-milling of HES material, prepared by co-precipitation, increases its specific capacity from 284 mAh g^{-1} to 492 mAh g^{-1} at a current density of 100 mA g^{-1} after 25 cycles. Besides, the smaller crystallite size reduces the volume changes in the materials during de-/lithiation.

1. Introduction

Recently, a new group of high-entropy oxide (**HEO**) materials with a spinel *Fd*-3 *m* structure obtained by solid-state reactions has been reported by Dąbrowa et al.[1] Typical spinels have the general structural formula (A$_{1-x}$B$_x$)$_{Td}$[A$_{x/2}$B$_{1-x/2}$]$_{Oh2}$O$_4$, where round and square brackets denote the tetrahedral (A site) and octahedral (B site) surroundings of metal ions, respectively. Here, the parameter x characterizes the degree of spinel inversion. When $x = 0$, the spinel structure is called "normal", (A^{2+})$_{Td}$[B^{3+}]$_{Oh2}$O$_4$, and when $x = 1$, it is called "inverse", (B^{3+})$_{Td}$[A$_{1/2}^{2+}$B$_{1/2}^{3+}$]$_{Oh2}$O$_4$. In the case of $0 < x < 1$, when the distribution of elements between sublattices is more complex, the spinel is called "partially inversed". The basic concept of the synthesis of HEO materials is the stabilization of the crystalline phase due to high configurational entropy, similar to high entropy alloys (**HEA**).[2,3] By achieving a high configurational entropy of the system, it is possible to obtain solid solutions at relatively low temperatures.[4,5] Again, when five or more elements are introduced into the cationic sublattices of spinel oxide, a high configurational entropy is achieved.[6,7] It is important to note

that one of the conditions for obtaining single-phase products the proximity of the ionic radii of cations to reduce microstresses and crystal lattice distortions.[8]

HEO spinels have interesting multifunctional properties that that allow them tob e used in catalysis,[9] electronics,[10] and energy storage.[5,11] It is worth noting that the magnetic properties of HEO spinels can be controlled by fine-tuning the morphology, chemical composition and local structure of the particles.[4,6,12] It was found that the catalytic properties of these oxides depend not only on the specific surface area, but also on the presence of oxygen vacancies O$_{vac}$ formed during synthesis at elevated temperatures.[13] Oxygen vacancies with high concentration can effectively increase the diffusion coefficient of lithium ions, thereby improving electrochemical properties of electrode materials.[14]

In 2018, a high-entropy oxide with a rock salt structure and the (Co,Cu,Mg,Ni,Zn)O composition was reported for the first time as an anode material for lithium-ion batteries.[15] However, in the rock-salt structure, most of the cations have an oxidation state of 2+, which limits the specific capacity of oxides of this type. Therefore, to increase the redox potential of cations, other structures were considered. The most promising are spinel-type structures in which the electrochemical process can involve several redox couples.[5,16,17] Among all the compositions, the most interesting is (Cr,Fe,Mn,Co,Ni)$_3$O$_4$ with equimolar ratio of cations.[1] It has a high specific capacity due to the participation of all redox couples in the electrochemical process. The de-/lithiation process takes place in accordance with the transformation mechanism. It is assumed that all constituent metals must be reduced to M^0. The reaction depth can be adjusted depending on the particle size.[9] Therefore, many authors use synthetic approaches that make it possible to obtain nanoparticles in a short period of time, which prevents agglomer-

[a] K. V. Mishchenko, P. Y. Tyapkin, A. B. Slobodyuk, N. V. Kosova
Siberian Branch of the Russian Academy of Sciences, Institute of Solid State Chemistry and Mechanochemistry, 18 Kutateladze, 630090 Novosibirsk, Russia
E-mail: kosova@solid.nsc.ru

[b] A. B. Slobodyuk
Far-Eastern Branch of the Russian Academy of Sciences, Institute of Chemistry, 159 pr. Stoletiya Vladivostoka, 690022 Vladivostok, Russia

[c] M. A. Kirsanova
Independent researcher, Moscow, Russia

📖 Supporting information for this article is available on the WWW under https://doi.org/10.1002/batt.202400350

Batteries & Supercaps

Research Article
doi.org/10.1002/batt.202400350

Chemistry
Europe
European Chemical
Societies Publishing

ation of particles. The following methods have been used to obtain HEO in the nanoscale state: flame spray pyrolysis, nebulised spray pyrolysis, solution combustion, microwave-assisted, reverse co-precipitation, hydrothermal, and oxidation of metal nanoparticles. Each method has its own advantages and disadvantages. For example, wet-chemical techniques have a higher potential for industrial applications than solid-state methods due to the scalability of the process. The advantage of co-precipitation is considered to be the production of a multicomponent system with a controlled pH of the solution. Another important fact is that the co-precipitation method allows all cations to be precipitated simultaneously into a mixed hydroxide with a uniform distribution of metal cations. However, the solid-state method remains the most cost effective, since it does not require repeated use and does not pollute wastewater.[1,5,8]

X-ray photoelectron spectroscopy (XPS) has revealed that the Mn, Fe and Co elements are distributed over both Oh and Td sites, while Ni and Cr prefer only Oh sites.[18] For example, in the case of nebulised spray pyrolysis, the oxide has the following composition: $(Co_{0.6}^{2.4+}Fe_{0.4}^{3+})(Cr_{0.3}^{3+}Fe_{0.1}^{3+}Mn_{0.3}^{2.9+}Ni_{0.3}^{2+})_2O_4$.[6] In the case of the solid-state synthesis, the distribution of elements for the tetrahedral site is $A=Mn_{0.06}^{2+}Fe_{0.33}^{3+}Co_{0.61}^{2+}$ and for the octahedral site is $B=Cr_{0.61}^{3+}Mn_{0.28}^{3+}Mn_{0.27}^{4+}Fe_{0.28}^{3+}Ni_{0.54}^{2+}$.[19] Moreover, even within the framework of the same synthesis method, there may be a difference in the values of the occupied positions of a particular cation or in the charge state of the cations. Therefore, it is difficult to obtain a HEO compound with the same distribution of elements.

In this work, we have carried out a comparative study of HEO spinels of nominal composition $(Cr,Fe,Mn,Co,Ni)_3O_4$ obtained by two different synthesis methods: co-precipitation and solid-state synthesis with preliminary ball-milling of reagents. The composition of the as-obtained samples, their local structure as well as their electrochemical properties were studied using a complex of physico-chemical methods. This work also shows the effect of ball-milling with carbon black on the specific capacity of HEO anode materials with different morphology and composition.

Experimental

Materials Synthesis

High-entropy spinels (HES) $(Cr,Fe,Mn,Co,Ni)_3O_4$ were prepared by mechanochemically assisted solid-state synthesis (hereafter, **HES**^{S}) and co-precipitation process (hereafter, **HES**^{C}). Stoichiometric amounts of Cr_2O_3 (99%, Reakhim), Fe_2O_3 (99.7%, Reakhim), MnO (99%, Alfa Aesar), Co_3O_4 (99%, Reakhim) and NiO (98%, Alfa Aesar) were used for solid-state synthesis. The mechanical activation (**MA**) of the stoichiometric reagent mixtures was carried out using a high-energy AGO-2 planetary mill with stainless steel jars and balls (the mass ratio of the samples and the balls was equal to 1:40) at 450 rpm in an Ar atmosphere for 5 min.

The following salts were used for the co-precipitation method: $Cr(CH_3COO)_3$ (98%, Reachim), $Fe(NO_3)_3 \cdot 9H_2O$ (98%, Reachim), $Mn(CH_3COO)_2 \cdot 4H_2O$ (99%, Sigma-Aldrich), $Co(NO_3)_2 \cdot 6H_2O$ (98%, Reachim) and $Ni(NO_3)_2 \cdot 6H_2O$ (98%, Reachim). The co-precipitation

process was carried out as follows: (i) the solution A was prepared by adding 50 ml of ammonia to 450 ml of distilled H_2O, (ii) $0.1 \, mol \, L^{-1}$ solution B with the equiatomic concentration of transition metals was prepared by adding an appropriate amount of soluble metal salt to 250 ml of distilled H_2O. In the next step, solution B was added drop by drop to solution A with continuous stirring of the mixture while maintaining a constant pH=10. After filtration and washing with water, the precursor precipitate was dried at 90°C for 6 h and ground in an agate mortar.

The mechanically activated oxide mixtures and hydroxide precursors were placed into agate crucibles and annealed at 773, 973, and 1273 K for 2 h in air followed by natural cooling to room temperature.

Materials Characterization

The as-prepared samples were characterized by X-ray powder diffraction (XRD), differential thermal analysis (DTA), scanning electron microscopy (SEM), transmission electron microscopy (TEM), Raman, Mössbauer and atomic absorption (AA) spectroscopy, and galvanostatic cycling. The phase composition of the precursors was studied by XRD, using a Bruker D8 Advance diffractometer, Cu Kα radiation ($\lambda = 1.5418$ Å). The XRD patterns were collected over the 2Θ range of 10–90° with a step of 0.02° s^{-1} and uptake time of 0.2 s. Structural refinement of the XRD parameters was carried out by the Rietveld method using the GSAS software package.

Thermal analysis of the released gaseous products was performed using a quadrupole mass spectrometer STA 449F3. Precursors were heated to 1273 K in an argon atmosphere with a heating rate of 10 K/min.

Particle size and morphology were investigated by SEM using a Hitachi TM-1000 scanning electron microscope and by TEM using an aberration-corrected Titan Themis Z transmission electron microscope equipped with a Super-X detection system and operated at 200 kV. Samples for TEM were prepared by dipping the holey Cu grids with a lacey carbon supporting layer into dry powder of the as-prepared samples. No solvent was used. Conventional TEM images, selected area electron diffraction (SAED) patterns, high-angle annular dark field scanning transmission electron microscopy (HAADF-STEM) and annular bright field scanning transmission electron microscopy (ABF-STEM) images were collected. Atomic-resolution STEM images were recorded at a semi-angle of convergence of 30 mrad and angular range of 57–200 mrad and 14–53 mrad for HAADF- and ABF-STEM detectors, respectively. Energy dispersive X-ray (EDX) maps and spectra were registered in the STEM mode using an embedded Super-X detection system.

Raman spectra were recorded on a single-stage Horiba LabRAM HR evolution spectrometer (Japan). Individual spectra were collected in the 100–900 cm^{-1} range. Atomic absorption (AA) spectroscopy analysis was performed using an Agilent AA280FS spectrometer (Varian, Inc, USA).

^{57}Fe Mössbauer spectra were recorded using an NZ-640 spectrometer (Hungary) operating in a constant acceleration mode with ^{57}Co (Rh) radioactive source at 298 K (RT) and 83 K (LT) using the SpectrRelax program.[20] The hyperfine magnetic field (H_{hf}) distribution ($p(H_{hf})$) was recovered for each Mössbauer spectrum. When the isomer (δ) and quadrupole (ε) shifts were also distributed, we believe that there is a linear correlation between these parameters and the hyperfine magnetic field. All spectra were fitted by pure Lorentz lines. Isomer shifts are given with respect to metallic iron. Studies of magnetic properties were carried out on a PPMS magnetometer (Quantum Design, USA) in the 2–380 K temperature range and the field induction up to 20 T.

For the electrochemical testing, the as-prepared samples were mixed with carbon black. The composite cathodes consist of 75 wt% of active material, 20 wt% of carbon black and 5 wt% of PVDF/NMP binder. The mixed slurry was applied to a Cu foil using doctor blade to obtain working electrodes. The working electrodes were dried at 363 K for 2 h in a vacuum, and then rolled. The loading density of the prepared samples was 2–3 mg cm^{-2}. The Swagelok-type cells were assembled in an argon-filled glove box (VBOX-SS 950, Vilitek, Russia) with Li as a counter electrode, 1 M LiPF$_6$ (Sigma Aldrich, 99.99%) solution in ethylene carbonate (EC) and dimethyl carbonate (DMC) (Alfa Aesar, 99%) in a ratio of 1:1 by weight as an electrolyte, and a glass fiber filter (Whatman, Grade GF/C) as a separator. Cycling was performed using a galvanostatic mode with a current density of 100 and 500 mA g^{-1} within the voltage range of 0.01–3.0 V vs. Li/Li$^+$ at room temperature using a Biologic BCS 805 battery cycling system.

2. Results and Discussion

2.1. X-Ray Diffraction

Figure 1 shows the XRD patterns of the samples with $(Cr,Fe,Mn,Co,Ni)_3O_4$ composition obtained by two methods: co-precipitation (HES^C) and mechanochemically assisted solid-state synthesis (HES^S) after annealing at 773, 973 and 1273 K for 2 h. It can be seen that the HES^S sample obtained from a mixture of transition metal oxides at 773 K shows reflections of the initial oxides and those belonging to the spinel phase.[21] The HES^C sample obtained at 773 K shows the reflections of the corresponding spinel, however with low intensity. The HES^C and HES^S samples prepared at higherer temperatures are single-phase spinels without any impurities. All reflections can be successfully indexed based on the cubic spinel structure with the space group Fd-$3m$ (# 227), which was confirmed by the electron diffraction.

However, there is a slight difference in the full width at half-maximum (FWHM) of the HES^C and HES^S reflections. The average crystallite size of the prepared samples was determined using the Scherrer Equation (1):

$$D = \frac{K\lambda}{\beta \cos \theta} \tag{1}$$

where D is the crystallite size, K is the shape factor (0.9 for the cubic lattice), λ is the wavelength (0.154 nm), β is the FWHM and θ is a peak position in radians. According to Equation (1), the crystal size is higher for the HES^C samples, while the decrease in the FWHM of diffraction peaks occurs due to an increase in the nucleation rate and lattice deformation caused by an increase in temperature.

To find out the reason for the broadening of reflections, microstrains formed in the crystal lattice, or the size effect, the dependence in the $\beta \cos \theta$ vs. $\sin \theta$ coordinates was plotted (Figure S1) using the W–H Equation (2):

$$\beta \cos \theta = \frac{K\lambda}{D} + 4\varepsilon \sin \theta \tag{2}$$

where β is the FWHM and θ is the peak position (in radians); K is the shape factor, λ is the wavelength (0.154 nm), D is the crystallite size (in nm) and ε is the microstrains of the crystal lattice. By drawing a line through a series of experimentally determined values of $\beta \cos\theta$, the slope of the line will be proportional to ε, and extrapolating the line to the y axis will give a value inverse to D. It can be seen that for the HES^C samples, D increases from 115–231 nm with an increase in the synthesis temperature from 773–1273 K (Figure S1). Significant deviations of the points from a straight line indicate that the microstructure of the sample is more complex due to the presence of defects. It is worth noting that microstrains were almost absent, when the sample was synthesized at 1273 K. For the HES^S sample, with increasing the synthesis temperature to 1273 K, the values D and ε change slightly and are equal to 198 nm and 0.0093, respectively.

To further understand the effect of crystallinity, crystallite size (CS) and lattice constant on the lattice distortion of HES obtained at different temperatures, the intensity ratio I_{220}/I_{311} was calculated, and the results are shown in Table 1. Lattice distortion can be qualitatively assessed by determining the experimental intensity ratio I_{220}/I_{311} to the intensity ratio of ideal spinel Fe_3O_4, equal to 0.29.[22] As the synthesis temperature increases from 973–1273 K, a decrease in the degree of structural distortion is observed. It is equal to 17% for HES^C and to 21% for HES^S.

The results of the structural refinement, including crystallographic XRD parameters, correlate with the literature data.[5,9,23] The lattice parameter a for the HES^C sample exceeds that for the HES^S sample (Table 1). This may be due to the formation of oxygen vacancies during high-temperature synthesis and, as a result, charge compensation of transition metal ions.[22,24]

Chemical analysis using SEM-EDX for the HES^C and HES^S samples obtained at 1273 K evidences a deviation from the nominal distribution of TM ions, which leads to the production of the following compositions: $(Cr_{0.20}Fe_{0.21}Mn_{0.24}Co_{0.20}Ni_{0.15})_3O_4$ for HES^C and $(Cr_{0.20}Fe_{0.18}Mn_{0.22}Co_{0.18}Ni_{0.22})_3O_4$ for HES^S. The element concentrations obtained by atomic absorption (**AA**)
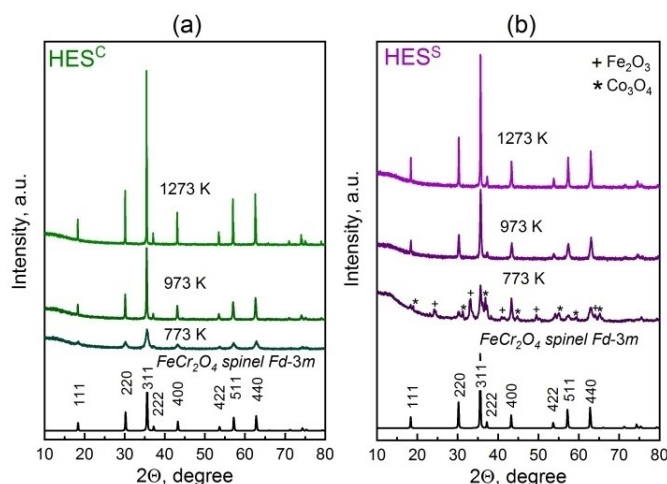

Figure 1. XRD patterns of the HES^C (a) and HES^S (b) samples prepared by annealing at 773, 973, and 1273 K.

Batteries & Supercaps

Research Article
doi.org/10.1002/batt.202400350

Chemistry Europe
European Chemical
Societies Publishing

Table 1. Rietveld refined lattice parameters of HES^C and HES^S prepared at different temperatures.

Space group Fd-3 m

Sample	T, K	a, Å	R_{wp}, %	GOF	CS, nm	$I_{220}/_{311}$	Lattice distortion, %
HES^C	1273	8.377(2)	8.11	1.67	254	0.34	17
HES^C	973	8.368(1)	7.49	1.07	50	0.38	31
HES^C	773	8.272(1)	7.92	1.12	21	0.44	52
HES^S	1273	8.328(1)	7.57	1.41	78	0.35	21
HES^S	973	8.326(1)	6.96	1.21	36	0.40	38
HES^C-BM	1273	8.368(1)	8.34	1.17	54	0.24	17
HES^S-BM	1273	8.335(2)	7.16	1.15	20	0.08	72

suggest that there is a nickel deficiency in the final product of HES^C ($(Cr_{0.22}Fe_{0.26}Mn_{0.17}Co_{0.27}Ni_{0.08})_3O_4$), whereas in HES^S, almost all elements are in the concentrations close to the original ones ($(Cr_{0.18}Fe_{0.21}Mn_{0.18}Co_{0.22}Ni_{0.21})_3O_4$). The Ni deficiency can be explained as follows: the stability of the metal complex increases with a decrease in the size of metal cations, and the stability of the complexes for M^{2+} ions increases in the following sequence $Ba^{2+} < Sr^{2+} < Ca^{2+} < Mg^{2+} < Mn^{2+} < Fe^{2+} < Co^{2+} < Ni^{2+} < Cu^{2+} < Zn^{2+}$. This stability trend is known as the Irving-Williams series.[25,26] Consequently, the resulting nickel ammonia complex will be more stable than the other metal complexes included in HES. In the "normal" spinel, the M^{2+} ions are located in the Td sites, but in the inverse spinel, they preferably occupy the Oh sites. Thus, it can be assumed that some ions with a preferred location in the Td sites, such as Fe^{3+}, Co^{2+}, Mn^{2+}, and Fe^{2+}, are able to replace them for the Oh sites to obtain partially inverse spinel.[27] Assuming that the Ni ions must be located in the Oh sites in this spinel, their deficiency may affect the redistribution of cations between sublattices.[19,28] As mentioned earlier, the lattice parameter of HES^C are larger than those of HES^S, therefore, based on the data in Table S1, it can be concluded that not only the oxidation state of the elements changes, but also the location of ions in the Td or Oh positions. Figure S2 shows the particle size distribution curves of the obtained HES^C and HES^S samples, followed by ball-milling (BM) for 5 min and subsequent BM for 1 min with 5% C, as well as XRD patterns of BM HES and SEM image of HES^S + BM 5% C. It can be seen that BM with carbon facilitates the grinding of the material and reduce its particle size.

containing nanoscale particles, while the HES^S sample was prepared by annealing the mechanically activated oxide mixture. The particles of the HES^C samples obtained at two different temperatures are very similar and consist of polygonal particles about 5 μm in size. However, as the temperature rises, large particles are destroyed, forming densely packed oxide grains of 0.5–1 μm in size. This effect is probably due to the decomposition of the as-obtained manganese dioxide with the simultaneous release of oxygen, while the TG curves show a gradual decrease in mass up to 1073 K. The particles of the HES^S sample obtained at 973 K have a submicron size, but it increases with increasing temperature (Figure S3).

TEM images of HES^C, prepared at 973 K, show the macro-sized agglomerates consisting of polygonal grains with size varying from 60–100 nm (Figure 2a). When the synthesis temperature of HES^C is raised to 1273 K, the average size of primary particles increases to 300–700 nm or even more (Figure 2b). Individual EDX maps in Figure 3 show a uniform distribution of elements by grain volume. The molar ratio Cr:Fe:Mn:Co:Ni = 0.252(6):0.250(10):0.213(11):0.229(5):0.057(1) calculated on the basis of STEM-EDX analysis is characterized by a significantly lower nickel content compared to the nominal ratio, which is consistent with the AA spectroscopy data. High-resolution HAADF-STEM images (Figure 4a and b) of the HES^C sample illustrate the atomic packing of the TM cations typical for the spinel structure. The SAED images, recorded simultaneously with HAADF-STEM, allow us to visualize both cationic and anionic sublattices (Figure 4c and d).
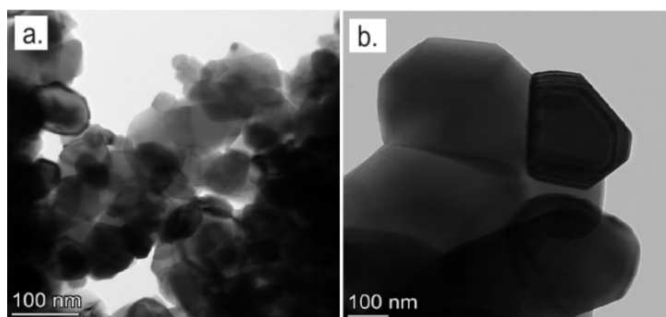
2.2. Electron Microscopy

The analysis of the particle size distribution shows that the amount of coarse fraction in the HES^C particles is significantly higher than that in the HES^S particles. And vice versa, the fraction of the fine particles in HES^S is much larger than that in HES^C, probably, due to different precursors used. To better understand the morphology and microstructure of HES, SEM and TEM studies were conducted.

Figure S3 presents SEM images of HES obtained at 973 and 1273 K using two different synthesis methods. The HES^C sample was obtained from an amorphous mixed hydroxide precursor

Figure 2. TEM images showing morphology and grain structure of HES^C particles obtained by annealing at 973 K (a) and 1273 K (b).

Batteries & Supercaps

Research Article
doi.org/10.1002/batt.202400350

Chemistry Europe
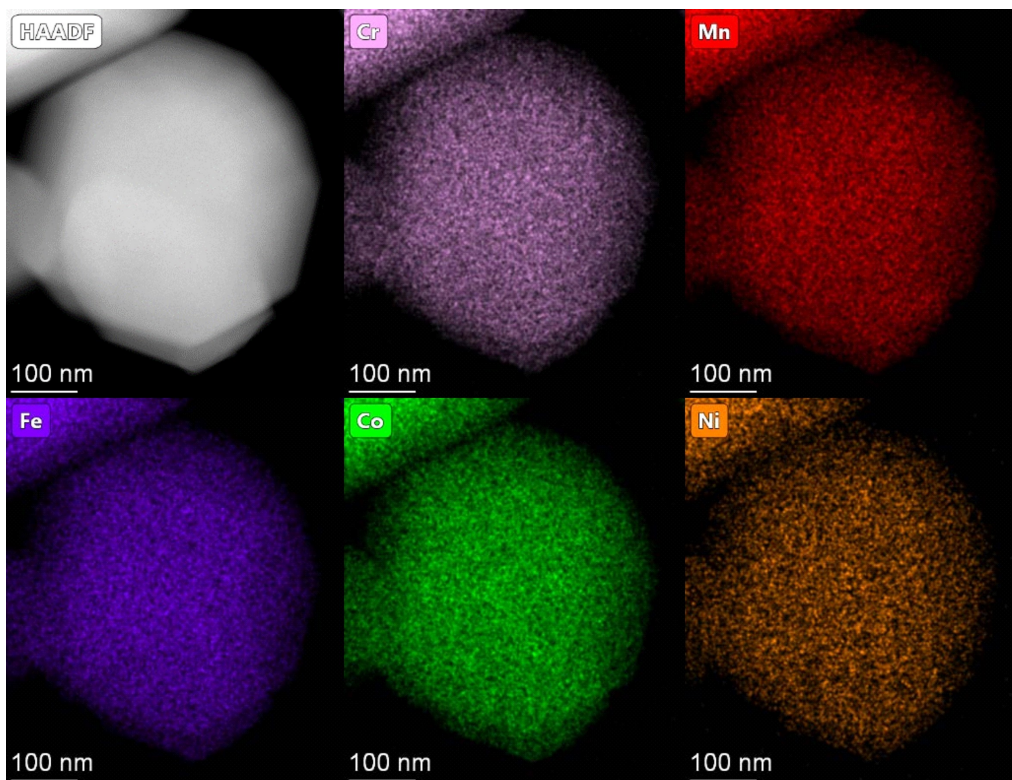European Chemical
Societies Publishing

Figure 3. Individual EDX maps of HES[C] particles obtained by annealing at 1273 K.
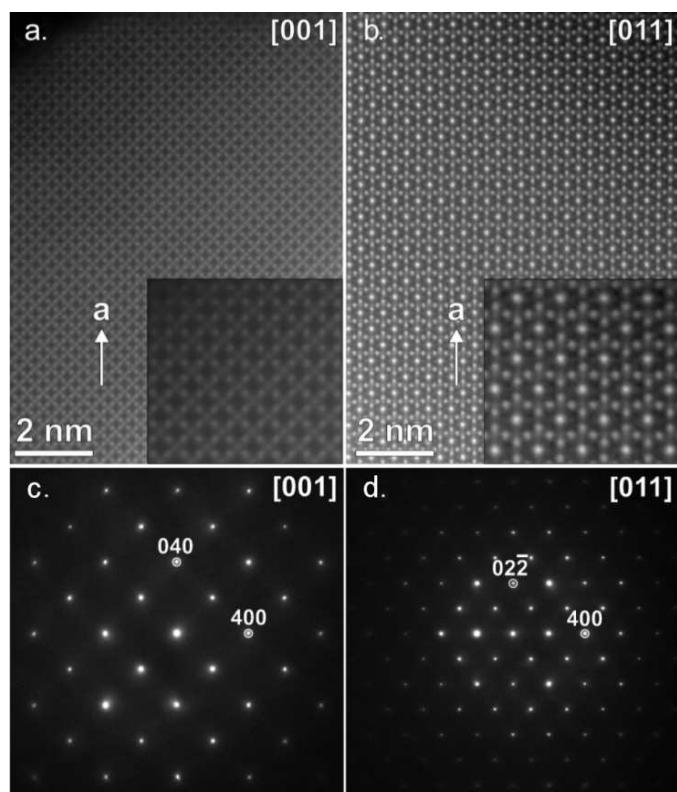

Figure 4. [001] (a) and [011] (b) HAADF-STEM and SAED images of HES[C] sample (1273 K) obtained along the main crystallographic directions (c, d) and indexed in *F*-centered cubic cell with *a* ~8.1 Å.

The molar ratio Cr:Fe:Mn:Co:Ni for HES[S] is equal to 0.188(9):0.212(8):0.208(12):0.197(3):0.195(2), that is, close to the nominal one. The SAED and HAADF-STEM images of the HES[S] sample are very similar to those of HES[C]. For HES particles obtained at a temperature of 973 K, a non-uniform distribution of elements is observed on the mixed EDX maps (Figures S4–S6).

2.3. Raman Spectroscopy

The structural properties of the as-prepared HES samples were also studied using Raman spectroscopy. The out-of-phase motion of atoms inside the crystal lattice leads to the appearance of lattice waves corresponding to modes of optical vibrational. These waves are easily excited by conventional spectroscopic methods, since they can interact with an applied external electric field. If the oscillation is accompanied by a change in polarizability, such a vibrational mode becomes Raman active. A change in the dipole moment leads to the appearance of infrared vibrations. The number of bands in the vibrational spectra of spinels strongly depends on the symmetry of the unit cell. For highly symmetric structures with cubic symmetry (space group *Fd*-3 *m*), the smallest number of bands in the spectrum is observed. According to the selection rule, only 5 modes: A_{1g}, E_g, and $(3)F_{2g}$ are active in the Raman spectra.[29] The assignment of bands to the corresponding vibrations of atoms in the spinel structure is often difficult due

Batteries & Supercaps

Research Article
doi.org/10.1002/batt.202400350

Chemistry
Europe
European Chemical
Societies Publishing

to the presence of a larger number of bands than predicted by the selection rule.[30,31]

This behavior has been the subject of numerous studies, but there is a general opinion that additional bands in the vibrational spectra of spinel appear due to the disorder effect.[32] The disorder can occur due to a complete or partial inversion of the spinel structure. In known systems, some of the A and B ions can be located in both octahedral and tetrahedral positions, and the degree of inversion can vary over a wide range depending on the chemical composition and the method of synthesis.[33,34] Disorder can also occur due to the replacement of one position by atoms with different oxidation states.[5]

Figure 5 shows that HES, crystallized in a cubic spinel structure, have active Raman bands from 100–800 cm^{-1}.[35] These results are in good agreement with the data obtained for similar HEO structures[1,9,36,37] and with the spectra of the $ZnCrO_4$, $MgFe_2O_4$, and $MgAl_2O_4$ spinels.[5,35,38–40] Intensive bands with wave numbers from 600 cm^{-1} to 700 cm^{-1} indicate the motion of A–O bonds in AO_4 tetrahedra, while bands from 100 cm^{-1} to 500 cm^{-1} indicate the motion of B–O bonds in BO_6 octahedra.[35] However, the Raman bands for HES^C sample have a shifted characteristic towards higher wavenumbers, while the opposite trend is observed for the HES^S sample. The differences in the corresponding values of the bandwidth intensity for the samples indicate the possibility of small deviations from the average chemical composition,[41] as well as the difference in the ionic radii of metals (electronic state) and M–O bond distance.[42]

For example, partial substitution of nickel in NiO for Fe^{3+} leads to a shift of the Raman band at 508 cm^{-1} to higher values,[43] and partial substitution of iron ions in Fe_3O_4 for Cr^{3+} leads to an increase in the intensity of the Raman band at 543 cm^{-1} and the appearance of a shoulder at 675 cm^{-1}.[41] The position of the peaks shifts to lower wavenumber values when the radius of the cation in the tetrahedral position increases as in the $NiFe_2O_4$ and $ZnFe_2O_4$ spinels, but the opposite effect is observed when the radius of the cation in the octahedral position increases.[35] The appearance of additional peaks may also indicate a decrease in symmetry or the formation of a superstructure with an increasing degree of freedom of vibrations.[30]

To refine the Raman spectra of HES, about ten bands are required, described by the Gauss and Lorentz functions (Tables S2–S6). The predominance of expanded peaks for the HES^C sample obtained at a temperature of 773 K reflects the disordered structure (or low crystallinity) with an inhomogeneous distribution of lattice defects.[10,44] The evident band shift indicates a redistribution of the intensity of the main bands with the bands resulting from the inversion.[35,36] In the case of metal oxidation to the trivalent state, the intensity of the A_{1g} mode decreases, and its shift to higher frequencies is associated with a decrease in the A–O bond in the AO_4 tetrahedra and the appearance of the A_{1g}' inverse mode.[9,22,35] With an increase in the synthesis temperature of HES^C, the intensity of the $F_{2g}(1)$ mode responsible for B–O bond vibrations in BO_6 octahedra decreases, while the intensity of the $F_{2g}'(1)$ inversion mode increases.[9] The intensive mode A_{1g}' of the HES^S sample obtained at 973 K indicates a higher degree of inversion in the tetrahedral positions, and when the synthesis temperature increases to 1273 K, the integral intensity of the E_g, $F_{2g}(2)$ and $F_{2g}(3)$ modes, corresponding to the octahedral sites of normal spinel, increases too.[36] Thus, the degree of HES^C spinel inversion increases when the amorphous precursor is heated, which can be associated with a change in the oxidation state of metals or the redistribution of cations between sublattices. The mixture of oxides forms a set of partially inverse spinels, which subsequently interact to form partially separated inverse spinels.[21] Interestingly, the degree of spinel inversion decreases when Co or Ni ions are replaced by diamagnetic Zn ions.[45] Thus, it can be assumed that the composition of HES^S is more variable.

2.4. Magnetic Properties

HES are characterized by a rather wide variety of magnetic properties, which strongly depend on both composition and morphology.[46] A common feature of the studied samples is the presence of magnetic ordering in their spin systems (Figure 6a). The curves of the dependence of magnetization on the field have hysteresis and indicate the ferrimagnetic nature of spin ordering (Figure 6c and d). The temperature dependence curve of magnetic susceptibility of HES^C and HES^S samples recorded in a weak field is similar to the literature data, including a saturation in the low temperature region and a decrease in magnetization near Neel temperature (T_N) at 380–400 K.[21,47]

The low-temperature parts of high-field susceptibility for the samples obtained by different methods have only a small discrepancy (Figure 6a). However, both their T_N and coercive force differ substantially. The coercive force of the HES^C sample
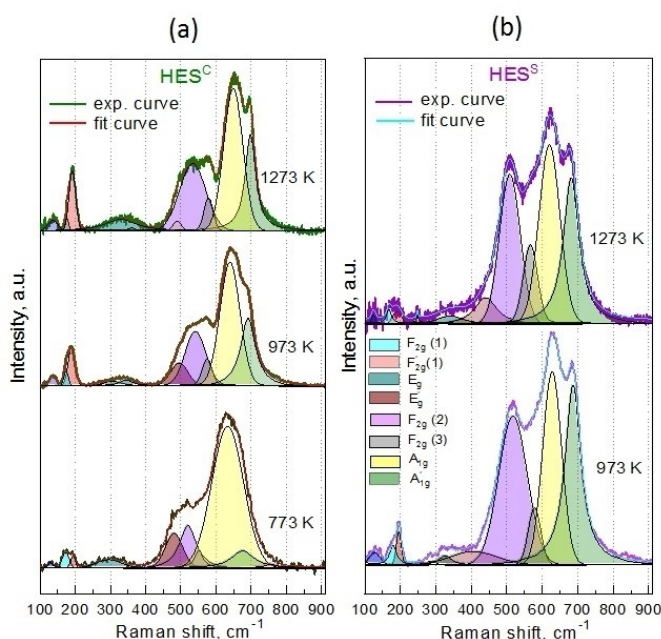

Figure 5. Raman spectra of HES^C (a) and HES^S (b) obtained at different temperatures.

Batteries & Supercaps

Research Article
doi.org/10.1002/batt.202400350

Chemistry Europe
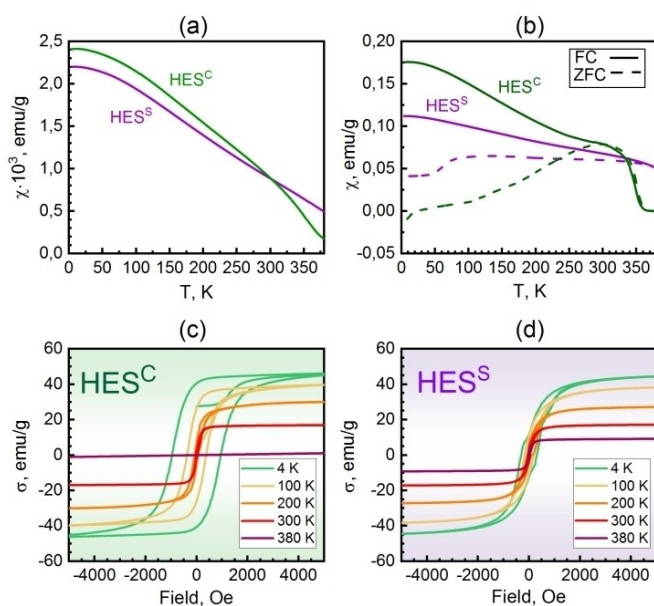European Chemical
Societies Publishing

Figure 6. Temperature dependences of the magnetic permeability of HES in the field of 20 kOe (a) and in the modes of field cooling (FC) and zero field cooling (ZFC) regimes (H = 100 Oe) (b). Magnetic hysteresis loops of HES^C (c) and HES^S (d) recorded at 4, 100, 200, 300, and 380 K.

single-domain particles, while HES^C particles have domain walls that impede the motion of spins due to larger coercive force.[48] It can also be noted that the field dependence of the magnetization of HES^S sample is characterized by the absence of complete saturation at 4 K (Figure 6d). This could be caused by the presence of superparamagnetic particles in this sample. The paramagnetic contribution can be estimated by fitting the curves with a sum of linear and Langevin functions, that gives nearly equal σ_{sat} values (48 and 51 emu g^{-1} for HES^C and HES^S samples, respectively). At 4 K, there is no paramagnetic contribution for HES^C, while for HES^S, a contribution of $117 \cdot 10^{-6}$ emu Oe^{-1} g^{-1} is observed.

2.5. Mössbauer Spectroscopy

The Mössbauer spectra of HES^S and HES^C heat treated at 1000 °C are given in Figure 7a–d, respectively. The fitting procedure of the HES spectra is difficult due to uncertainty both in the number of partial spectra and in the values of their parameters. First of all, there is a significant uncertainty in determining the relative amounts of iron cations in a certain oxygen environment. This is especially noticeable for RT spectra, characterized by a wide distribution of hyperfine fields (Figure 8a–d).
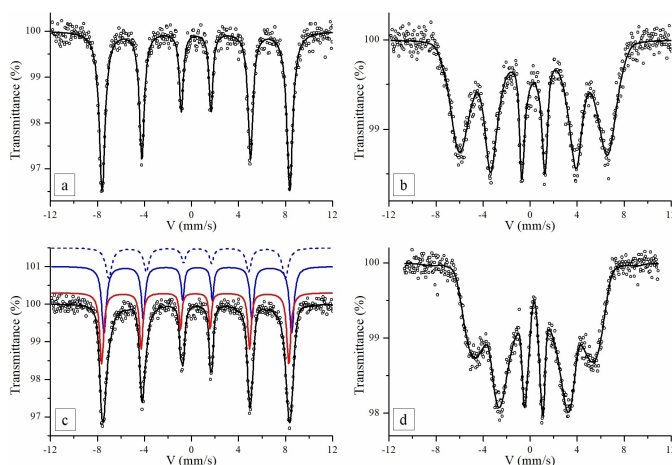
(956 Oe at 4 K) is much higher than that of HES^S sample (305 Oe), which is manifested in a noticeable difference between the field cooling (FC) and zero field cooling (ZFC) curves (Figure 6b) and the hysteresis loop areas (Figure 6c and d). It is known that the types and temperature regions of magnetic transitions depend on the location of cations in A and B sublattices of antiferromagnetic spinels.[4,28] The addition of non-magnetic ions can increase the total magnetization due to their preferential occupation of positions A and the associated compensation loss of the magnetic moment between the sublattices. The substitution also reduces the transition temperature.[48] The amount of Ni ions in HES^C is significantly lower compared to HES^S, and its substitution with another metal leads to a change in the magnetic behavior of the system. The difference in grain structure between the samples, confirmed by the TEM images of the particles, may be another factor that determines different magnetic properties of the samples. The HES^S sample may contain a significant number of

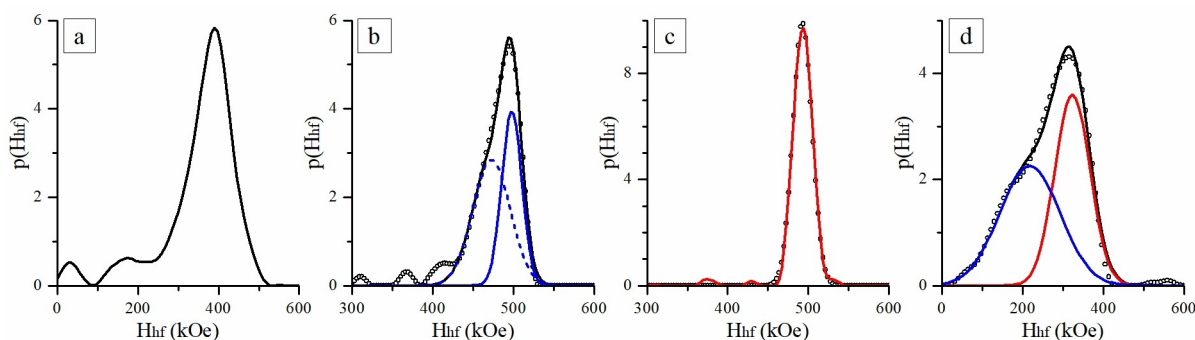**Figure 7.** LT (a, c) and RT (b, d) Mössbauer spectra of HES^S (a, b) and HES^C (c, d).

Figure 8. The distributions p(Hhf) of the hyperfine magnetic field Hhf obtained from the spectra of HES^S (a –298 K) and HES^C (b, c –83 K, d –298 K).

Batteries & Supercaps

Research Article
doi.org/10.1002/batt.202400350

Chemistry Europe
European Chemical
Societies Publishing

If we consider a case that is not in the close vicinity of the Neel point, then the hyperfine field distribution can be caused by the contribution of super-exchange interactions arising from all the nearest neighboring cations interacting with the iron atoms through oxygen p-orbitals.[49] In spinel ferrites, atoms in oxygen tetrahedra (site [A]) are adjacent to 12 octahedral [B]-atoms, while those in site [B] are adjacent to 6[A]- and 6[B]-atoms.[50] However, the B—O—B bonds form a 90° angle, so, these interactions are less favorable from a magnetic point of view and we can only take into account the contribution of A—O—B bonds. The difference in the set of neighboring cations leads to a difference in the local magnetic fields on the iron nuclei. Another option, superparamagnetic relaxation, is due to the fact that the magnetic moment of single-domain particles jumps from one light axis to another. The process accelerates with increasing temperature, leading to a decrease in the hyperfine field and broadening of spectral lines.

The LT spectrum of the HES^S sample (Figure 7a) fits quite well by a single sextet with $\delta = 0.389$ mm s^{-1} and $H_{hf} = 495$ kOe (Table 2). However, the RT spectrum (Figure 7b) fits much worse.

To identify the reasons of such behavior, we restored the distribution of hyperfine parameters (Figure 8a). Line broadening is apparently related to the distribution of hyperfine fields which demonstrate the presence of components with low H_{hf} values of about 180 and 30 kOe, while isomer and quadrupole shifts seem to be poorly distributed. Taking into account the small size of the coherent-scattering region (78 nm, Table 1) for this sample, these low-field components can be associated with various small particles exhibiting superparamagnetic behavior. The main component of the distribution looks quite symmetrical and is characterized by $\delta = 0.284$ mm s^{-1} and $H_{hf} = 389.9$ kOe. Its half-width (in terms of field) is relatively high (about 100 kOe), so we can conclude that it is caused not only by the difference in the nearest neighbor cations and affects the magnitude of the local hyperfine field due to super-exchange interactions, but also by the superparamagnetic relaxation of single-domain particles. Since we did not find a significant distribution of isomer shifts in the LT and RT spectra, we assume that iron cations are located, if not completely, but at least predominantly in the positions [A], since the values of these shifts are typical for iron cations in a tetrahedral oxygen environment.

The LT spectrum of the HES^C sample (Figure 7c) can be fitted by two or more partial subspectra with different isomer shifts. To establish the required number of components, we have constructed two distributions of hyperfine fields, assuming a clear separation of isomer and quadrupole shifts (Figure 8b and c). Then, we decomposed these distributions and obtained three different sites (two octahedral and one tetrahedral) for iron cations. Based on this model, we decomposed the original Mössbauer spectrum. The Mössbauer parameters are given in Table 3. One tetrahedral ($\delta = 0.321$ mm s^{-1}) and one octahedral ($\delta = 0.527$ mm s^{-1}) components seem to have almost the same hyperfine field (about 495 kOe) as for HES^S. The remaining component ($\delta = 0.494$ mm s^{-1}) has a slightly smaller H_{hf} value of 466 kOe, while half-width of the corresponding distribution is about 50 kOe. We came to the conclusion that this component describes several nonequivalent local states of iron cations located in the [B] sites, but differing from each other by the amount of special next-nearest neighbors, probably, chromium atoms that weaken A—O—B superexchange interactions.[49,51] Several sets with different relative occupancies of atoms between [A] and [B] sites were calculated in Ref. [50] The most favorable configuration of elements is $(Cr_{0.35}Fe_{0.35}Mn_{0.05}Co_{0.05}Ni_{0.2})(Cr_{0.125}Fe_{0.125}Mn_{.275}Co_{.275}Ni_{0.2})_2O_4$, where Cr atoms preferentially occupy [A] sites, while Co atoms occupy [B] sites, that is consistent with our conclusion. Another possibility is the presence of ordered cation vacancies in the tetrahedral sublattice due to a lack of Ni cations.

Table 2. Mössbauer parameters of the HES^S spectra (Figure 7a and b).

T, K	δ, mm·s^{-1}	ε, mm·s^{-1}	H_{hf}, kOe
83	0.389 ± 0.005	0.008 ± 0.005	495.0 ± 1.0
298	0.284 ± 0.021*	0.004 ± 0.026*	389.9 ± 1.6*

δ–isomer shift, ε–quadrupole shift, H_h–hyperfine field, Γ_i–half-widths of sextet lines (1–outer, 2–middle, 3–inner lines). *Mössbauer parameters (δ, ε, H_{hf}) refer to the maximum of the distribution (Figure 8a).

Table 3. Mössbauer parameters of the HES^C spectra (Figure 7c, d).

T, K	A, %	δ, mm/s	ε, mm/s	H_{hf}, kOe
83	39 ± 7	0.527 ± 0.016	0.013 ± 0.005	495.0 ± 1.0
	24 ± 4	0.494 ± 0.011	0.020 ± 0.010	466.0 ± 2.0
	37 ± 6	0.321 ± 0.012	0.006 ± 0.005	494.0 ± 1.0
83	59 ± 6	0.508 ± 0.012	0.016 ± 0.009	[a]498.0 ± 1.0
				[a]473.0 ± 7.0
	41 ± 6	0.352 ± 0.010	0.022 ± 0.007	[a]493.0 ± 1.0
298	52 ± 5	[b]0.344 ± 0.005	[b]0.011 ± 0.005	[b]218.0 ± 9.0
	48 ± 5	[b]0.311 ± 0.005	[b]0.003 ± 0.005	[b]323.1 ± 1.5

δ – isomer shift, ε – quadrupole shift, H_{hf} – hyperfine field, Γ_i – half-widths of sextet lines, A –relative area. [a]Hyperfine fields are calculated based on decomposition of their distributions (Figures 8b,c). [b]Mössbauer parameters (δ, ε, H_{hf}) are calculated based on decomposition of their distributions (Figure 8d).

Batteries & Supercaps

Research Article
doi.org/10.1002/batt.202400350

Chemistry Europe
European Chemical
Societies Publishing

The RT spectrum (Figure 7d) demonstrates a bimodal distribution of hyperfine parameters (Figure 8d). Thus, there are only two components with $H_{hf} = 218$ kOe and $H_{hf} = 323.1$ kOe, slightly different by the values of the isomeric shift (0.344 mm s^{-1} and 0.311 mm s^{-1}, respectively). Such situation is typical for γ-Fe$_2$O$_3$. At room temperature, it is often impossible to normally separate the sites of iron cations due to rather similar values of isomer shifts, equal to about 0.3–0.34 mm s^{-1}.[52,53] However, near the liquid nitrogen temperature, the difference between isomer shifts can reach the values of about 0.2 mm s^{-1}.[53] If the hypothesis about the presence of vacancies in the sublattice [A] is correct, then the disorder at room temperature may explain the absence of two distinct local states of iron in the octahedral sublattice.

Thus, both samples tend to contain only Fe^{3+} cations, which preferentially occupy the [A] sites. Rearrangement of cations can occur both due to the low concentration of point defects, which can probably stabilize the structure of HES in the form of small particles, as in HES^S, or due to leakage of some element, for example, nickel, as it happens with HES^C.

2.6. Electrochemical Performance

The electrochemical properties of HES were investigated in a galvanostatic mode within the 3.0–0.01 V at the current density of 100 mA g^{-1} and 500 mA g^{-1} and room temperature (Figures 9 and Figures S7–S9). The theoretical capacities of 1074 mAh g^{-1} and 993 mAh g^{-1} for HES^C and HES^S, respectively, were calculated based on the AA data.

Five initial galvanostatic discharge/charge curves measured at 100 mA g^{-1} for HES^C and at 500 mA g^{-1} for HES^S are shown in Figure 9a and b, respectively. It can be seen that the discharge/charge curves of HES have a shape typical for all HEO. The first lithiation curves are characterized by a potential plateaus at 0.4 and 0.5 V for HES^C and HES^S, respectively, which is associated with the electrolyte decomposition, while the formation of the solid electrolyte interphase on the surface of HES^S can be explained by the presence of more Ni, which has a tendency to the oxidation of other transition metals in HES^C, such as Co or Cr, which contributes to the intercalation of a large amount of Li and increases the specific capacity.[54] Interestingly, the HES^S sample demonstrates the highest specific capacity of 1352 mAh g^{-1} at 500 mA g^{-1} instead of 1166 mAh g^{-1} for HES^C (Figure 9d). However, all samples are characterized by a rapid drop in capacity. The cycling stability of the HES electrodes was estimated, and the data obtained for 25 cycles at 100 mA g^{-1} and 500 mA g^{-1} for both samples are shown in Figure 9c and d. The HES^C sample shows the best result when cycling for a long time at a current density of 100 mA g^{-1}. At higher current density of 500 mA g^{-1}, this sample shows a rapid drop in capacity compared to HES^S. This difference in electrode behavior is probably related to the morphological and structural changes in HES. It is known that the SEI layer apparently becomes harmful to small particles faster than to large ones.[55]

Discharge/charge profiles of the samples annealed at 773 and 973 K are very similar, and an irreversible discharge capacity is observed after the first cycle (Figures S7–S9). However, the HES^C sample shows higher specific capacity as well as more stable cycling than the HES^S sample (Figure 10). Since there is a need to obtain HEO nanoparticles for wide
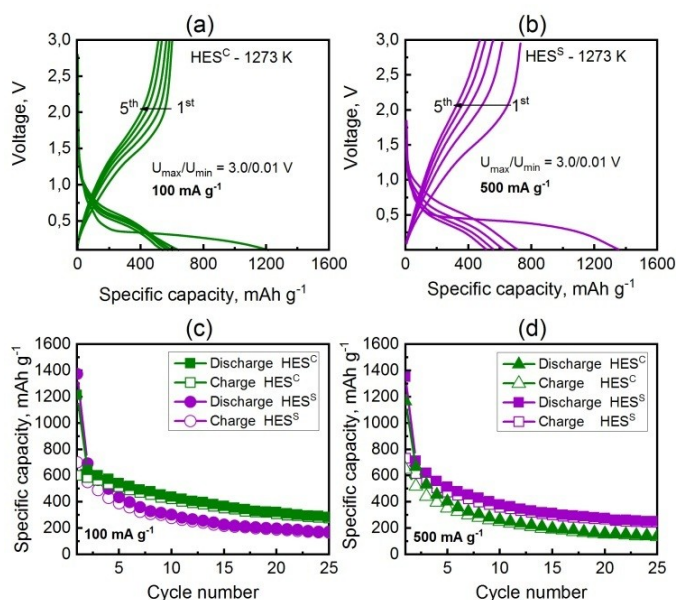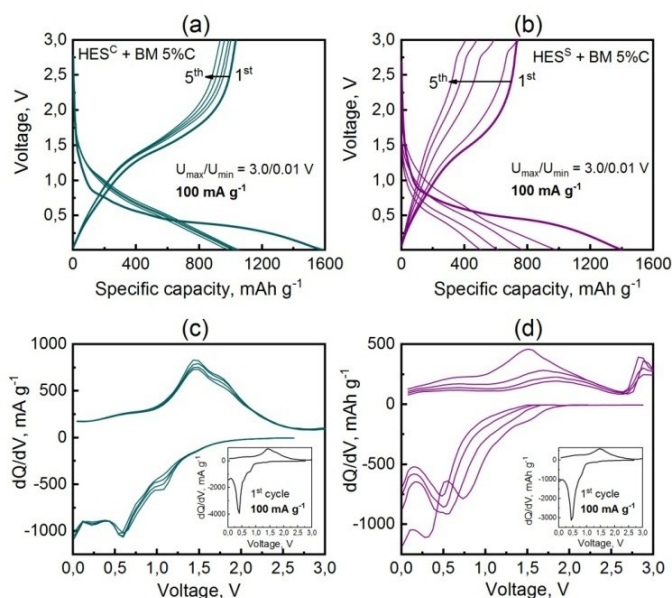

Figure 9. Electrochemical performance of HES annealed at 1273 K. Discharge/charge profiles of HES^C (a) and HES^S (b) samples; the dependence of specific capacity versus the cycle number of HES^C and HES^S at 100 mA g^{-1} (c) and 500 mA g^{-1} (d).

Figure 10. Electrochemical performance of HES^C (a) and HES^S (b) samples annealed at 1273 K with subsequent BM with 5% C. Galvanostatic discharge/charge profiles measured at 100 mA g^{-1} and corresponding differential capacities versus voltage plots over five cycles (c and d).

Batteries & Supercaps

Research Article
doi.org/10.1002/batt.202400350

Chemistry
Europe
European Chemical
Societies Publishing

applications such as LIBs or catalysis,[13,56,57] repeated ball-milling (BM) can be successfully used to reduce the particle size. An increase in the specific surface area of particles can have a positive effect on the physico-chemical properties of the HEO samples.[37,58] The repeated BM of these samples for 5 min leads to significant deviations of the experimental points from a straight line with a decrease in particle size and an increase in microstrains. After BM of HES, the number of submicron particles increases significantly, but a small amount of particles with a size of 50–70 μm remains in the samples (Figure S2a and S2b). The data obtained by granulometry are confirmed by XRD and SEM data (Figure S2c and S2d). According to the Scherrer's equation (Equation (1)), the calculated crystallite size decreases to 54 and 20 nm for ball-milled HES^C and HES^S, respectively (Table 1). So, to increase the electronic conductivity, conductive composites were obtained by subsequent BM of HES with amorphous carbon black (5%) for 1 min.

Figure 10 shows the discharge/charge curves and differential capacities versus voltage plots at a current density of 100 mA g^{-1} for HES^C and HES^S obtained after BM with 5% C. As shown in Figure 10a and b, there is a clear voltage plateau at about 0.5 V for the first discharge of both samples, which represents the reduction of metal oxide and the formation of SEI layer and agrees well with the differential curves (Figure 10c and d). The initial discharge/charge specific capacities of HES^C and HES^S are equal to 1591/1033 mAh g^{-1} and 1352/730 mAh g^{-1}, respectively. With subsequent cycling, a slope appeared instead of a plateau, which is associated with structural rearrangement and different reactions of various metals.[59] The discharge/charge curves of HES^C after BM (Figure 10a) are similar to those before BM (Figure 9a), which indicates a similar electrochemical process. As shown in Figure 11, all samples suffer from a drop in capacity with an increase in current density. A decrease in capacity at high current occurs due to kinetic limitations of diffusion-induced processes during delithiation. HES^C delivers the best performance after 25 cycles with a high specific capacity of 492 mAh g^{-1} and 330 mAh g^{-1} at a current density of 100 mA g^{-1} and 500 mA g^{-1}, respectively. These results are similar to previous tests of oxide anodes.[60]

Ex situ XRD studies (Figure 12) show that after 100 cycles, the diffraction peaks of the spinel structure are no longer visible due to the formation of small crystallites. These results coincide
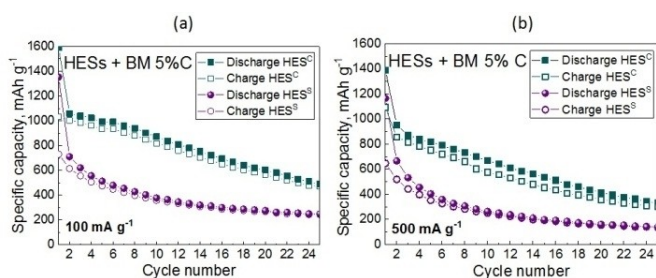

Figure 12. Ex situ XRD patterns of the initial HES^C and HES^S samples and after 100 cycles of galvanostatic charge-discharge.

with the results obtained in other works.[59,61,62] The presence of weak XRD signals indicates the role of phase stabilization effects in HES caused by high entropy. Due to the mobility of the A and B sites in the spinel structure, more spinel combinations can be expected. For example, in, Ref. [59] the phase separation of pristine HES into two new spinel phases, namely, $Cr_xFe_{3-x}O_4$ and $LiNi_xCo_{1-x}O_2$, was observed. Apparently, similar thermodynamically stable phases are formed in our case: in HES^C, it is mainly a phase with a large cell parameter, while in HES^S, it has a smaller one. These phases act as structural stabilizers and are obviously responsible for the cyclability of the electrodes.

3. Conclusions

Thus, high-entropy spinel-type oxides $(Cr_{0.22}Fe_{0.26}Mn_{0.17}Co_{0.27}Ni_{0.08})_3O_4$ and $(Cr_{0.18}Fe_{0.21}Mn_{0.18}Co_{0.22}Ni_{0.21})_3O_4$ were obtained by co-precipitation and solid-state synthesis, respectively, and evaluated as anode materials for LIBs. XRD, Raman and TEM results confirm the single-phase spinel structure (space group Fd-3m) for both samples obtained after annealing at 973 and 1273 K. Based on the EDX and XRD data, with an increase in the synthesis temperature, the cations are more evenly distributed over the sublattices, the crystallite size increases and the lattice distortion decreases. The magnetic properties of spinels can be controlled using synthesis conditions and fine-tuning not only the grain size, but also the ratio of non-magnetic and magnetic ions. The results of Mössbauer spectroscopy show that in all HES, the valence state of the Fe ions is 3+, while an insufficient amount of nickel leads to its redistribution over A and B sublattices. It should be noted that a large fraction of Fe^{3+} cations in tetrahedral sites leads to a higher degree of inversion in $(Cr_{0.18}Fe_{0.21}Mn_{0.18}Co_{0.22}Ni_{0.21})_3O_4$. The electrochemical results show that although all ball-milled HES generally have good cyclabil-

Figure 11. The dependence of the specific capacity versus the cycle number of HES samples annealed at 1273 K with subsequent ball milling (BM) with 5% C at 100 mA g^{-1} (a) and 500 mA g^{-1} (b).
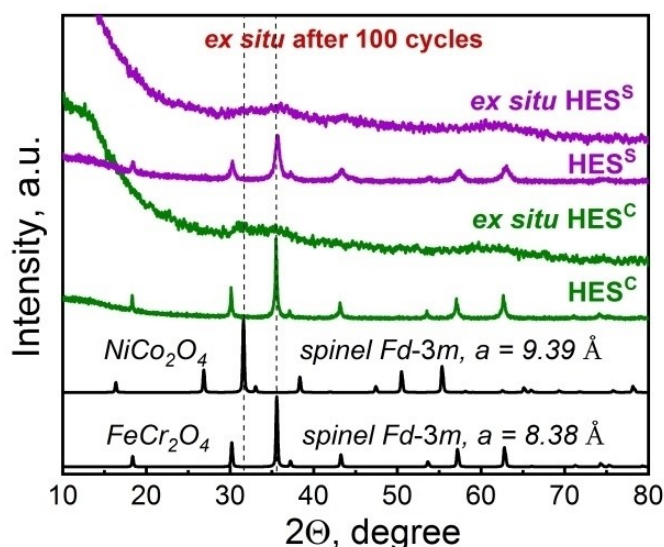
ity, the $(Cr_{0.22}Fe_{0.26}Mn_{0.17}Co_{0.27}Ni_{0.08})_3O_4$ electrode has the best performance. Moreover, this sample ball-milled with 5% C shows the capacity of $492\ mAh\,g^{-1}$ and $330\ mAh\,g^{-1}$ after 25 cycles at a current density of $100\ mA\,g^{-1}$ and $500\ mA\,g^{-1}$, respectively. However, for untreated samples, this behavior deteriorates significantly. After cycling for 100 cycles, high-entropy spinels decompose into thermodynamically stable low-entropy Cr/Fe and Ni/Co spinel phases. It is worth noting that the $(Cr_{0.22}Fe_{0.26}Mn_{0.17}Co_{0.27}Ni_{0.08})_3O_4$ sample has the largest lattice parameter and demonstrates the best electrochemical properties, which allows it to be used not only in Li^+-ion, but also in Na^+-ion batteries.

Author Contributions

The manuscript was written through contributions of all authors. K.V.M. – materials synthesis and characterization, electrochemical studies, writing – original draft preparation. P.Yu.T. – Mössbauer spectroscopy study. A.B.S. – NMR spectroscopy study. M.A.K. – transmission electron microscopy study. N.V.K. – conceptualization, methodology, writing – review and editing, supervision. All authors have given approval to the final version of the manuscript.

Conflict of Interests

The authors declare no conflict of interest.

Data Availability Statement

The data that support the findings of this study are available from the corresponding author upon reasonable request.

[1] J. Dąbrowa, M. Stygar, A. Mikuła, A. Knapik, K. Mroczka, W. Tejchman, M. Danielewski, M. Martin, *Mater. Lett.* **2018**, *216*, 32.

[2] C. M. Rost, E. Sachet, T. Borman, A. Moballegh, E. C. Dickey, D. Hou, J. L. Jones, S. Curtarolo, J.-P. Maria, *Nat. Commun.* **2015**, *6*, 8485.

[3] B. Cantor, I. T. H. Chang, P. Knight, A. J. B. Vincent, *Mater. Sci. Eng. A* **2004**, *375–377*, 213.

[4] S. Dai, M. Li, X. Wang, H. Zhu, Y. Zhao, Z. Wu, *J. Magn. Magn. Mater.* **2021**, *536*, 168123.

[5] D. Wang, S. Jiang, C. Duan, J. Mao, Y. Dong, K. Dong, Z. Wang, S. Luo, Y. Liu, X. Qi, *J. Alloys Compd.* **2020**, *844*, 156158.

[6] A. Sarkar, B. Eggert, R. Witte, J. Lill, L. Velasco, Q. Wang, J. Sonar, K. Ollefs, S. S. Bhattacharya, R. A. Brand, H. Wende, F. M. F. de Groot, O. Clemens, H. Hahn, R. Kruk, *Acta Mater.* **2022**, *226*, 117581.

[7] Y. Zheng, X. Wu, X. Lan, R. Hu, *Processes* **2022**, *10*, 49.

[8] M. Stygar, J. Dąbrowa, M. Moździerz, M. Zajusz, W. Skubida, K. Mroczka, K. Berent, K. Świerczek, M. Danielewski, *J. Eur. Ceram. Soc.* **2020**, *40*, 1644.

[9] D. Wang, Z. Liu, S. Du, Y. Zhang, H. Li, Z. Xiao, W. Chen, R. Chen, Y. Wang, Y. Zou, S. Wang, *J. Mater. Chem. A* **2019**, *7*, 24211.

[10] B. Talluri, M. L. Aparna, N. Sreenivasulu, S. S. Bhattacharya, T. Thomas, *J. Energy Storage* **2021**, *42*, 103004.

[11] T.-Y. Chen, S.-Y. Wang, C.-H. Kuo, S.-C. Huang, M.-H. Lin, C.-H. Li, H.-Y. T. Chen, C.-C. Wang, Y.-F. Liao, C.-C. Lin, Y.-M. Chang, J.-W. Yeh, S.-J. Lin, T.-Y. Chen, H.-Y. Chen, *J. Mater. Chem. A* **2020**, *8*, 21756.

[12] A. Mao, H.-Z. Xiang, Z.-G. Zhang, K. Koji, H. Zhang, Y. Jia, *J. Magn. Magn. Mater.* **2020**, *497*, 165884.

[13] L. Yuan, C. Xu, S. Zhang, M. Yu, X. Wang, Y. Chen, L. Dai, *J. Colloid Interface Sci.* **2023**, *640*, 359.

[14] B. Xiao, G. Wu, T. Wang, Z. Wei, Z. Xie, Y. Sui, J. Qi, F. Wei, X. Zhang, L. Tang, J. Zheng, *ACS Appl. Mater. Interfaces* **2023**, *15*, 2792.

[15] A. Sarkar, L. Velasco, D. Wang, Q. Wang, G. Talasila, L. Biasi, C. Kübel, T. Brezesinski, S. S. Bhattacharya, H. Hahn, B. Breitung, *Nat. Commun.* **2018**, *9*, 3400.

[16] X.-F. Luo, J. Patra, W.-T. Chuang, T. X. Nguyen, J.-M. Ting, J. Li, C.-W. Pao, J.-K. Chang, *Adv. Sci.* **2022**, *9*, 2201219.

[17] H. Minouei, N. Tsvetkov, M. Kheradmandfard, J. Han, D.-E. Kim, S. I. Hong, *J. Power Sources* **2022**, *549*, 232041.

[18] S. K. Shaw, A. Gangwar, A. Sharma, S. K. Alla, S. Kavita, M. Vasundhara, S. S. Meena, P. Maiti, N. K. Prasad, *J. Alloys Compd.* **2021**, *878*, 160269.

[19] G. H. J. Johnstone, M. U. González-Rivas, K. M. Taddei, R. Sutarto, G. A. Sawatzky, R. J. Green, M. Oudah, A. M. Hallas, *J. Am. Chem. Soc.* **2022**, *144*, 20590.

[20] M. E. Matsnev, V. S. Rusakov, *AIP Conf. Proc., Am. Ins. Phys.* **2012**, *1489*, 178.

[21] Y.-T. Yeh, C.-W. Huang, A.-Y. Hou, C.-Y. Huang, Y.-D. Lin, W.-W. Wu, *Small* **2023**, *20*, 2307284.

[22] X. Sun, X. Zeng, X. He, W. Fang, X. Du, W. Li, L. Zhao, H. Chen, *J. Alloys Compd.* **2022**, *925*, 166560.

[23] J. Wang, D. Stenzel, R. Azmi, S. Najib, K. Wang, J. Jeong, A. Sarkar, Q. Wang, P. A. Sukkurji, T. Bergfeldt, M. Botros, J. Maibach, H. Hahn, T. Brezesinski, B. Breitung, *Electrochemistry* **2020**, *1*, 60.

[24] Z. Grzesik, G. Smoła, M. Miszczak, M. Stygar, J. Dąbrowa, M. Zajusz, K. Świerczek, M. Danielewski, *J. Eur. Ceram. Soc.* **2020**, *40*, 835.

[25] P. R. Varadwaj, A. Varadwaj, B.-Y. Jin, *Phys. Chem. Chem. Phys.* **2015**, *17*, 805.

[26] T. Chmielewski, J. Wódka, Ł. Iwachów, *Physicochemical Problems of Mineral Processes* **2009**, *43*, 5.

[27] A. Navrotsky, O. J. Kleppa, *J. Inorg. Nucl. Chem.* **1967**, *29*, 2701.

[28] S. K. Shaw, P. Kumari, A. Sharma, N. Jatav, A. Gangwar, N. S. Anuraag, P. Rajput, S. Kavita, S. S. Meena, M. Vasundharai, I. Sinha, N. K. Prasad, *Physica B + C* **2023**, *652*, 414653.

[29] B. Nandan, M. C. Bhatnagar, S. C. Kashyap, *J. Phys. Chem. Solids* **2019**, *129*, 298.

[30] C. V. Ramana, M. Massot, C. M. Julien, *Surf. Interface Anal.* **2005**, *37*, 412.

[31] Z. Wang, P. Lazor, S. K. Saxena, H. St, C. O'Neill, *Mater. Res. Bull.* **2002**, *37*, 1589.

[32] M. Maczk, M. Ptak, M. Kurnatowska, J. Hanuza, *Mater. Chem. Phys.* **2013**, *138*, 682.

[33] P. Thibaudeau, F. Gervais, *J. Phys. Condens. Matter* **2002**, *14*, 3543.

[34] N. V. Minh, I. S. Yang, *Vib. Spectrosc.* **2004**, *35*, 93.

[35] V. D'Ippolito, G. B. Andreozzi, D. Bersani, P. P. Lottici, *J. Raman Spectrosc.* **2015**, *46*, 1255.

[36] C. Triolo, M. Maisuradze, M. Li, Y. Liu, A. Ponti, G. Pagot, V. D. Noto, G. Aquilanti, N. Pinna, M. Giorgetti, S. Santangelo, *Small* **2023**, *19*, 2304585.

[37] A. Ponti, C. Triolo, B. Petrovičova', A. M. Ferretti, G. Pagot, W. Xu, V. D. Noto, N. Pinna, S. Santangelo, *Phys. Chem. Chem. Phys.* **2023**, *25*, 2212.

[38] H. Cynn, S. K. Sharma, T. F. Cooney, M. Nicol, *Phys. Rev. B* **1992**, *45*, 500.

[39] Z. Wang, P. Lazor, S. K. Saxena, G. Artioli, *J. Solid State Chem.* **2002**, *165*, 165.

[40] J. Kaczmarczyk, F. Zasada, J. Janas, P. Indyka, W. Piskorz, A. Kotarba, Z. Sojka, *ACS Catal.* **2016**, *6*, 1235.

[41] K. F. Mccarty, D. R. Boehme, *J. Solid State Chem.* **1989**, *79*, 19.

[42] A. Ahlawat, V. G. Sathe, *J. Raman Spectrosc.* **2011**, *42*, 1087.

[43] Z. Qiua, Y. Ma, T. Edvinsson, *Nano Energy* **2019**, *66*, 104118.

[44] J. Zuo, C. Xu, B. Hou, C. Wang, Y. Xie, Y. Qian, *J. Raman Spectrosc.* **1996**, *27*, 921.

[45] C. Triolo, S. Schweidler, L. Lin, G. Pagot, V. D. Noto, B. Breitung, S. Santangelo, *Energy Adv.* **2023**, *2*, 667.

[46] A. Mao, F. Quan, H.-Z. Xiang, Z.-G. Zhang, K. Kuramoto, A.-L. Xia, *J. Mol. Struct.* **2019**, *1194*, 11.

[47] B. Musicó, Q. Wright, T. Z. Ward, A. Grutter, E. Arenholz, D. Gilbert, D. Mandrus, V. Keppens, *Phys. Rev. Mater.* **2019**, *3*, 104416.

[48] D. S. Birajdar, D. R. Mane, S. S. More, V. B. Kawade, K. M. Jadhav, *Mater. Lett.* **2005**, *59*, 2981.

[49] J. B. Goodenough, *Magnetism and the Chemical Bond, Vol. 68*, Interscience Publishers, New York, London **1963**, 996.

[50] J. Cieslak, M. Reissner, K. Berent, J. Dabrowa, M. Stygar, M. Mozdzierz, M. Zajusz, *Acta Mater.* **2021**, *206*, 116600.

[51] N. K. Gill, R. K. Puri, *Spectrochim. Acta Part A* **1985**, *41*(8), 1005.

[52] R. Zboril, M. Mashlan, D. Petridis, *Chem. Mater.* **2002**, *14*(3), 969.

[53] S. J. Oh, D. C. Cook, H. E. Townsend, *Hyperfine Interact.* **1998**, *112*, 59.

[54] P. Poizot, S. Laruelle, S. Grugeon, L. Dupont, J.-M. Tarascon, *Nature* **2000**, *407*, 496.

[55] P. Poizot, S. Laruelle, S. Grugeon, L. Dupont, J.-M. Tarascon, *J. Power Sources* **2001**, *97–98*, 235.

[56] T. X. Nguyen, C.-C. Tsai, J. Patra, O. Clemens, J.-K. Chang, J.-M. Ting, *Chem. Eng. J.* **2022**, *430*, 132658.

[57] Y. Ma, Y. Zhang, Y. Jian, Z. Jiang, S. Chai, L. Li, L. Xia, C. He, *Fuel* **2023**, *353*, 129171.

[58] B. Petrovicovà, W. Xu, M. G. Musolino, F. Pantò, S. Patanè, N. Pinna, S. Santangelo, C. Triolo, *Appl. Sci.* **2022**, *12*, 5965.

[59] C.-Y. Huang, C.-W. Huang, M.-C. Wu, J. Patra, T. X. Nguyen, M.-T. Chang, O. Clemens, J.-M. Ting, J. Li, J.-K. Chang, W.-W. Wu, *Chem. Eng. J.* **2021**, *420*, 129838.

[60] H.-Z. Xiang, H.-X. Xie, Y.-X. Chen, H. Zhang, A. Mao, C.-H. Zheng, *J. Mater. Sci.* **2021**, *56*, 8127.

[61] T. X. Nguyen, J. Patra, J.-K. Chang, J.-M. Ting, *J. Mater. Chem. A* **2020**, *8*, 18963.

[62] C. Q. Duan, K. Tian, X. Li, D. Wang, H. Sun, R. Zheng, Z. Wang, Y. Liu, *Ceram. Int.* **2021**, *47*, 32025.